Nanostructures design by plasma afterglow-assisted oxidation of iron–copper thin films

A. Imam, A. Boileau, T. Gries, J. Ghanbaja, D. Mangin, K. Hussein, H. Sezen, M. Amati, T. Belmonte

Nanostructures design by plasma afterglow-assisted oxidation of iron–copper thin films

A. Imam[1], A. Boileau[1], T. Gries[1,2], J. Ghanbaja[1], D. Mangin[1], K. Hussein[3], H.Sezen,[4] M. Amati[4], T. Belmonte[1,2,*]

[1]Université de Lorraine, Institut Jean Lamour, UMR CNRS 7198, NANCY, F-54042, France

[2]CNRS, Institut Jean Lamour, UMR CNRS 7198, NANCY, F-54042, France

[3]Faculty of Science, section III, Department of applied physics, Lebanese University, Tripoli, Lebanon.

[4]Elettra - Sincrotrone Trieste S.C.p.A. S.S. 14 Km 163,5 in AREA Science Park, 34149 Basovizza, Trieste, Italy

* corresponding author. Email: thierry.belmonte@univ-lorraine.fr

ABSTRACT

Oxidizing thin films made of Fe–Cu alloy with an Ar–O_2 micro-afterglow operated at atmospheric pressure shows remarkable growth processes. The presence of iron in copper up to about 50% leads to the synthesis of CuO nanostructures (nanowalls, nanotowers and nanowires). Nanotowers show the presence of an amorphous phase trapped between crystalline domains. Beyond 50%, Fe_2O_3 iron nanoblades are also found. CuO nanowires as small as 5 nm in diameter can be synthesized. Thanks to the presence of patterned domains induced by buckling, it was possible to show that the stress level decreases when the iron content in the alloy increases. Iron blades grow from the inner Fe_2O_3 layer through the overlying CuO if it is thin enough.

KEYWORDS

B1. Oxides, B1. Nanomaterials, A1. Nanostructures, A1. Growth models

1. INTRODUCTION

Iron–copper alloys can be considered as simple model materials of solid-solution alloys beyond 873 K because the two metals are only slightly soluble into each other and do not form any other intermediate phase [1]. Below this threshold temperature, iron and copper do not mix. On the contrary, in the Fe–Cu–O ternary system, besides simple oxides (Cu_2O, CuO, FeO, Fe_3O_4 and Fe_2O_3), it is possible to synthesize the $CuFe_2O_4$ spinel phase whose principal decomposition by-product under reduced atmosphere is $CuFeO_2$, which exhibits the so-called delafossite structure [2]. The $Cu_6Fe_3O_7$ is not expected to be obtained below 1073 K [3]. $CuFe_2O_4$ crystallizes either in a tetragonal (stable at low temperature) or cubic (stable above 633 K) symmetry. Synthesis temperature above 973 K is usually required for the preparation of copper ferrite [4]. However, $CuO/CuFe_2O_4$ thin films could be obtained by *ex situ* oxidation in air at 723 K for 12 h from various starting metal/oxide nanocomposites deposited by radio-frequency sputtering [5].

Thermal oxidation of Fe–Cu alloys was studied mainly beyond 873 K [3, 6, 7]. By controlling the oxygen partial pressure to a sufficiently low level, Niu *et al.* [6] could avoid oxidation of copper for treatment temperatures ranging from 1073 to 1173 K. In these specific conditions, these authors showed that the scaling rates of the alloys were lower than for pure iron and decreased with an increase in the copper content at constant temperature. In a similar study, Li *et al.* [7] observed a specific behaviour between 873 and 1073 K in the case of magnetron sputtered Fe-Cu mixtures with nanometric grain size against cast alloy with identical composition but with larger grains. A grain size reduction promotes a selective external oxidation of iron, *i.e.* the more reactive element with regard to oxygen. It is due to an increase in the mutual solubility of the two components associated with the alloy preparation and the presence of a large density of grain boundaries. These boundaries behave as diffusion short-circuits, allowing a faster outward diffusion of iron during oxidation. Then, an iron-depleted region is present in a subsurface alloy layer.

To the best of our knowledge, no nanostructures have been synthesized yet by gas oxidation of Fe-Cu alloys. In the case of brass, the co-synthesis of ZnO–CuO nanostructures was made by directly heating the alloy in air [8].

Low-temperature oxidation favours anisotropic crystal growth, and thus, the synthesis of nanostructures. The role played by stress on outward diffusion of metallic ions is essential and affects to a certain extent the growth mechanisms [9, 10]. Resorting to non-equilibrium media like plasmas is known as being a way to provide a part of the total energy under a non-thermal form [11, 12]. Plasma synthesis of metal oxide nanostructures was widely investigated [13–26]. In direct low-pressure plasma processes, sputtering mechanisms can be partly responsible for the growth of nanostructures [13–15]. In plasma afterglow processes, active species like oxygen atoms or metastable states of oxygen – mainly the singlet state $O_2(a^1\Delta_g)$ – are available. They are more active than ground state oxygen at low temperature because of the extra amount of energy coming from dissociation or excitation. Oxidation of metals in these conditions promotes the growth of oxide nanostructures [21–26].

In the present work, oxidation of Fe-Cu alloys by a microwave afterglow at atmospheric pressure is investigated. As in ref. [8], the synthesis of nanostructures of two metallic oxides on the same spot is expected (*i.e.* Fe_2O_3–CuO here versus ZnO–CuO in ref. [8]). We also wish to observe and clarify the mutual influence of metallic elements on the growth mechanisms, a question that is still pending in the literature.

2. EXPERIMENTAL SET-UP

The experimental set-up is depicted in **figure 1a**. An atmospheric Ar–O_2 microwave plasma was ignited in a fused silica tube (27 mm inner diameter) placed in a 2.45 GHz resonant cavity. The power absorbed by the plasma was 100 W. Flow rates of gases were controlled by mass flow controllers and the total flow rate was 275 sccm (standard cubic centimeter per minute). The partial pressure of oxygen in the gas mixture was set at 9.1 vol.%. The treatment time was 2 hours. This is typically the duration of thermal oxidation treatments. The micro-

afterglow was visible during the first two minutes thanks to nitrogen impurities coming from the air and flowing through the plasma. It appears as a light beam escaping a hole (500 µm in diameter) drilled in a brass plate screwed on one wall of the cavity (**figure 1b**) [22]. After a couple of minutes, the afterglow emission becomes very weak and similar to a low-pressure argon-oxygen afterglow with water as trace impurity. Oxidizing active species in the afterglow are mainly O, $O_2(a)$ and $O_2(X)$ because the afterglow is too hot to allow the formation of O_3.

Samples were Fe–Cu films deposited by DC magnetron sputtering. The amount of copper and iron was set by adjusting the power applied to each metallic target. The thickness of the alloy layer was about 1 µm. The base vacuum in the sputtering chamber was 5×10^{-6} mbar. The distance between the sample, made of fused silica, and the targets (50 mm in diameter, 3 mm thick and > 99.99 % purity for Cu target and 0.25 mm and 99.5 % purity for Fe target) was 100 mm. The substrate-holder rotated at 28 revolutions per minute during deposition to ensure homogeneity. Thin films were deposited at a pressure of 5.8×10^{-3} mbar in a 10 vol% H_2 – 90 vol% Ar mixture. Before deposition, a shutter was placed in front of the target to isolate the substrate during 5 min in order to remove native oxide layers. Thin films were deposited without external heating and the deposition temperatures were below 50°C. About half an hour was needed to obtain a 1 µm thick coating.

Surface temperature has a key role in the growth of nanostructures. The temperature of the micro-afterglow was determined thanks to the $OH(A^2\Sigma^+;\ v' = 0 - X^2\Pi;\ v'' = 0)$ rotational spectrum recorded at 306.4 nm by optical emission spectroscopy with an iCCD camera (see ref. [22] for details). Typically, the rotational temperature in the present conditions was 1400 ± 50 K at the exit of the nozzle. Thus, the heat flux transferred to the fused silica substrate coated by a thin Cu/Fe layer was determined. Next, a heat-transfer model had to be used to estimate the temperature distribution on the surface of the fused silica exposed to the afterglow (for a complete description of the model, see ref. [23]). Indeed, the temperature at

this particular location could not be determined experimentally because of the too short distance between the substrate and the resonant cavity (3 mm here), direct infrared camera measurements being impossible to perform. Then, only the temperature of the rear side of the sample was measurable. With this experimental data and the numerical model, the surface temperature could be evaluated. The emissivity of the surface of a smooth, transparent fused silica sample was determined independently in the range [300 K–900 K] at wavelengths between 7.5 and 13 μm. Indeed, in the range of wavelengths, the emissivity varies strongly [27]. Using a Linkam THMS600 heating stage, we found $\varepsilon \approx 0.69$ over the whole probed spectral range. This value was in good agreement with published data [27].

Infrared camera measurements, performed on the rear side of the sample, were recorded with a FLIR A-300 thermal imaging camera. No significant temperature variation could be observed according to whether a 900 nm thick Fe–Cu layer, regardless of its composition, was present or not.

The calculated temperature gradient along the sample surface is given as supporting information (see supplemental material 1). At steady state, which is reached after about five minutes typically, the maximum temperature of the rear side of the sample is slightly below 723 K. On the front side, the temperature is hardly superior (less than 5-10 K as determined from unreported modelling results: here $T < 733$ K). So, we will consider that the treatment temperature is the same as the temperature of the rear side at the same radial position.

Treated surfaces were characterized by several surface diagnostics. Scanning Electron Microscopy (SEM) was made with a Philips XL 30. X-ray diffraction using Co-Kα radiation ($\lambda = 0.179026$ nm) was performed with a Bruker D8 Discover diffractometer. To perform localized analyses, θ/θ measurement with the parallel beam geometry and a beam collimator of 300 μm as a diameter was used. In this configuration, the analyzed area is limited to a maximum of 300 μm × 1 mm in the 2θ range scanned and the depth of the sample probed by X-rays is estimated to range from 1 to 3 μm. Transmission electron microscopy (TEM)

investigation was performed on as-grown nano-objects with a JEOL ARM 200F – Cold FEG TEM/STEM running at 200 kV (point resolution 0.19 nm) fitted with a GIF Quatum ER. A CAMECA IMS 7F instrument was used for Secondary Ion Mass Spectrometry (SIMS). A Cs^+ primary ion beam of 30 nA operating at 5 kV was used to sputter sample with an impact energy of 3 keV. Mass Resolving Power was set to 2000. Depth-profiles were acquired over an area of 100×100 μm^2.

3. RESULTS AND DISCUSSION

3.1. Structures of oxide layers

When the plasma afterglow, which behaves as a beam of active oxygen species (**figure 1b**), hits the metallic surface, it oxidizes concentric areas that extend radially up to several millimetres (**figure 1c**). Because of the temperature gradient that prevails in such conditions, Fe–Cu thin films, when submitted to the afterglow treatment, produce different nanostructures versus the radial distance for a given alloy composition. For a set of experimental conditions, results are very repeatable. The nanostructures are also strongly dependent on the film composition. Then, results concerning the oxidation of pure metals are presented separately in **figure 2**.

Oxidation of pure copper by the plasma afterglow gives from the centre of the treatment outward 3D architectures: spheres with nanowalls, nanowalls and nanowires [21]. Contrary to the nanowalls grown from Cu–Fe alloys, those produced here are homogeneous and no amorphous subdomains, as described hereinafter, are observable. On the other hand, oxidation of pure iron produces in the centre of the treatment hemispherical nanowalls together with nanoblades. Nanoblades are 2D nanowalls that are much higher than wide (at least by a factor of 3). These blades become thinner and thinner when one moves radially outward and resemble flat nanowires (which might be named also nanoribbons) far enough from the centre. Since they have a very recognisable shape of blades, the term "nanoblade" will be kept for these structures. Indeed, according to Wen *et al.* [28], Fe_2O_3 nanowires are much

straighter and their cross section becomes cylindrical only if the temperature is beyond 1073 K.

In **figure 3**, a map of the different nanostructures obtained with the afterglow process for iron contents ranging from 10 to 90% is depicted. Four main types of nano-objects are found: Fe_2O_3 nanoblades and CuO nanowalls, nanotowers and nanowires. High-resolution SEM images for CuO nanotowers and nanowalls are provided together with TEM images of the four identified nanostructures in **figure 4**. Their chemical composition is justified hereinafter. CuO nanowalls are characterized by their thickness, which is much larger than Fe_2O_3 nanoblades (~50 nm vs ~10 nm), their height, which is always lower than nanoblades for given conditions, and by their structure. Indeed, CuO nanowalls exhibit amorphous domains embedded in a crystalline matrix, which makes them look like as if they were porous (see SEM image in **figure 4**). This feature will be described in detai hereinafter. Nanotowers are intermediate structures between walls and nanowires: when the width of the wall shrinks, large steps appear along the height of the nanostructure, producing a serrated shape as in a tower. They can be described as an assembly of two narrow walls joined by an intermediate phase (see SEM image in **figure 4**). Sometimes, they also look like as if they were porous. TEM analyses prove undoubtedly that this appearance is due to the coexistence of amorphous and crystalline phases (**figure 5**) within the nanostructure, which seems to be subjected to instabilities, as if the outward metallic ion flux that feeds the nanostructure growth would occur intermittently. It is clear that the amorphous phase is embedded within the crystalline one (**figures 5b and 5c**). Near the interface between the two phases, crystalline nano-domains can even be discerned in the amorphous phase (**figure 5d**). The EDX mapping of these nanostructures (**figure 6**) indicates that both phases, the amorphous and the crystalline, are made of the same oxide, *i.e.* copper oxide. Unreported micro-diffraction patterns showed that this copper oxide is CuO. Detectable traces of iron, inferior to 1 at.% typically, are found (see results of micro-energy dispersive spectroscopy analyses in **supplemental material 2**).

When the alloy composition is 54% Fe-46%Cu, CuO nanowires with diameters as small as 5 nm are obtained. This is much lower than diameters of nanowires obtained by thermal oxidation or even by afterglow oxidation [21]. Indeed, according to Choopun *et al.* (see Table 1 on page 98 in ref. [29]), average diameters are most often larger than 20-30 nm.

For alloy compositions with less than 72% Fe, stress-induced patterns are observed (grey area in **figure 3**). Domains with an elliptic shape, the smaller as the iron content increases or the temperature decreases, are found. In **figure 7a**, a cross section image shows the pleated layer, which leads to patterns observed in **figure 7b**. From **figures 7a and 7c**, we notice that shorter nanowires grow on hills and longer ones in valleys. The level of stress being higher in valleys [30, 31], the same finding as Chen's [31] applies here: the higher the stress, the faster the growth rate. There is a direct evidence of the influence of stress on the growth rate. In the present conditions where the treatment temperature is low, diffusion occurs at grain boundaries. Their size and the level of stress are expected to affect not only the growth rate, but also the growth mechanism of the nanostructures to a certain extent, as discussed hereinafter.

Whatever the layer composition, as it is confirmed by space-resolved X-ray diffraction, no spinel phase ($CuFeO_2$, $CuFe_2O_4$ or $Cu_6Fe_3O_7$) was formed in our conditions (see **supplemental material 3**). The lack of FeO peaks in XRD patterns is likely due to the disproportionation of this phase into iron and Fe_3O_4, which occurs below 850 K [6]. CuO and Fe_2O_3 nanostructures were obtained, but no oxide containing both metallic elements (at least with concentrations higher than 1%, as discussed previously). The synthesis of spinel phases is probably impossible because the maximum temperature always remains below 733 K. The micro-afterglow is likely too cold.

In **figure 8**, we present SIMS results recorded every millimetre from the centre of a treated sample outward. The example of an alloy containing 34% Fe is given. Other data corresponding to the various compositions studied in this work are available in **supplemental**

material 4. Normalized intensities of Cu, Fe and O SIMS signals are depicted as a function of depth, defined with respect to the surface of the silica substrate on which PVD coatings were deposited. The sputtering time of the oxidized layer by the argon beam of the SIMS device cannot be simply converted into a thickness scale because of the strong changes in composition, density and structure throughout the layer. We also chose to present raw intensities, and not phase proportions, the oxygen signal being difficult to interpret in terms of oxidation levels of each metallic element. This is due to the specificity of the SIMS technique where the emission yield of one element is strongly affected by its environment. Besides, Kirkendall's porosity likely affects raw intensities according to the sample depth.

Cu and Fe signals evolve strongly as a function of the radial position. As the temperature decreases from the centre of the treatment outward, the farthest spots are less oxidized. Thanks to the mass difference between Fe and Cu, back-scattered electron images are useful to correlate the SIMS profiles to the structure of a specific stack of layers (**figure 8b**). At +5 mm, an outer copper oxide layer covers a Fe/Cu oxidized layer. Nanostructures are too sparse to affect significantly the SIMS profile at the chosen sputtering rate. They appear as a rise of the copper signal on the topmost part of the SIMS profile (segment [AB] in **figure 8b**). In the centre of the treatment, this layer of nanostructures is separated from the internal Fe/Cu oxidized layer in contact with fused silica (segment [EF]) by:

- a layer depleted in copper (segment [DE]) above which one finds
- a layer with small grains – as shown hereafter – (segment [CD]) and
- a columnar layer (segment [BC]) almost made of pure copper.

The internal Fe/Cu oxidized layer (segment [EF]) is extremely porous, because of the accumulation of vacancies. Vacancies are due to the outward diffusion of metal cations and aggregate to create the so-called Kirkendall porosity. This internal layer is likely made of sub-layers too, as far as the copper and iron profiles show it, but because of the huge porosity of this layer, it seems tricky to assert it.

When we move from the centre of the treatment outward (**figure 8a**), we observe from SIMS profiles that the main modification of the film is the shrinkage of layer [DE], which is characterized by a depletion in copper that becomes less and less pronounced. Other layers ([BC] and [CD]) are still present, even though their sizes decrease too, justifying thus a smooth evolution of the CuO nanowalls to the copper nanotowers and then nanowires, from +1 to +5 mm. In **figure 9**, a magnification of the topmost layers is useful to describe phenomena at stake in the synthesis of CuO nanostructures. The layer depleted in copper (segment [DE]) is characterized by large grains with pores. Above it, a layer with small grains (segment [CD]) contains a mixture of copper and iron. It supports a columnar layer (segment [BC]) almost made of pure copper, which is characterized by the fact that each column has approximately the diameter of the nanostructures found in layer [AB]. Magnifications a) and b) in **figure 9**, show that the roots of the CuO nanostructures do correspond to columns in layer [BC]). In particular, **figure 9b** also shows that several columns can grow side by side as a whole, producing a nanotower with amorphous boundaries between columns, like in nanowires depicted in **figure 5d**. The same growth mechanism applies for CuO nanowalls, as shown in **figure 10**. Note that CuO nanowalls are visible in this cross-section view but not Fe_2O_3 nanoblades. We observe in the case of an iron-rich alloy (90% in Fe), that the layer of nanostructures [AC] here, *i.e.* the former [AB] layer, and layer [CD] are still visible, whereas layer [BC] is no longer present. Layer [CD] is extremely thin and can hardly be observed in **figure 10**. It is also difficult to observe it in the SIMS profile in which only one inflection point is visible. However, it is present. This is clearer for a 72%-iron rich alloy where this layer is thicker (**figure 11**). The point is that nanowalls seem to grow directly on this buffer layer [CD], without any contact with large grains of the [DE] layer. This was systematically observed over a large number of examples.

Among CuO nanowalls, Fe_2O_3 nanoblades can be observed. Patently, the mean width of the hematite blades is much larger than that of CuO nanowalls, suggesting a different growth mechanism (**figure 12**).

3.2. Growth mechanisms

Voss *et al.* [32] proposed a growth mechanism of hematite nanoblades. In the α-Fe_2O_3 layer, the grain size is relatively small and has considerable intergranular porosity. Surface diffusion along these intergranular pores and grain boundary diffusion combine to provide transport of Fe through the α-Fe_2O_3/Fe_3O_4 interface. Blades grow from the tip [28, 32, 33] and this indicates that surface diffusion of Fe in α-Fe_2O_3 is much faster than O. According to Bertrand *et al.* [34], the rate controlling step of the overall oxidation rate is the cationic diffusion in the external magnetite layer, which is the thickest layer with the largest grain size. However, significant diffusion of oxygen through α-Fe_2O_3 occurs along grain boundaries. The primary mechanism for α-Fe_2O_3 blade growth is therefore surface diffusion along a central tunnel. Twin defects are observed in all blades formed above 973 K but they probably play a minor role in the transport of Fe atoms. According to Wen *et al.* [28], what is called nanobelts (*i.e.* narrow nanoblades) grow from defects such as planar defects of twins and grain boundaries. These authors describe a temperature-dependence of the shape of the nanostructures which is opposite of our results. At low temperature (near 673 K), surface oxidation mainly produces hematite nanowalls (here, they were obtained at or slightly below the highest temperature, ~733 K). At 873 K, structures similar to the present nanoblades start growing due to the increased diffusion rate of Fe in the defect sites (here these nanostructures were found below 623 K). When the temperature increases to 973 K, the increased diffusion rate of Fe significantly facilitates the hematite nanobelt growth (here, they were obtained at lower temperature than the nanowalls). Finally, when the temperature is set at 1073 K, the nanowires are much straighter and their cross section becomes cylindrical (here, temperatures were lower and then, no Fe_2O_3 nanowires were obtained in our conditions). From the specific

behaviour observed for alloys in our conditions (at least, with respect to Wen *et al.*'s results), we infer that layer [CD] must be thin enough to let iron from layer [DE] with large grains cross the topmost copper oxide layer and reach the surface to form nanoblades. Otherwise, iron remains buried under the topmost copper layer. Basically, the difference between Wen *et al.*'s results and ours is a matter of shape of 2D-nanostructures. Then, we assume that the shape of the blades or walls is not controlled by the temperature directly, but by other parameters like the grain size, the level of stress or even the nature of the oxidizing species, which might act on surface reconstruction processes.

The role of stress on the growth of nanostructures is essential. Indeed, stress speeds up diffusion processes. This means that for a given growth rate, the temperature can be lowered. Then, the lowering of the temperature affects the anisotropy of diffusion. It also affects the grain size of the thus-formed oxides. The lower the temperature, the lower the grain size. In **figure 9**, a SEM cross-section view of the growing oxide is shown together with the corresponding SIMS depth-profile. The presence of iron in copper leads to a segregation of metallic elements: the topmost surface (layer [BC]) is made of Cu oxide and it is characterized by columnar grains. The layer underneath (layer [DC]) is essentially composed of copper oxide, the iron content starting to increase, and made of small grains. Still below, layer [DE] containing both metallic elements exhibits a large-grain structure with apparent pores. Diffusion of copper to the top of the scale layer requires diffusion through the small-grain sublayer [CD] from the underlying reservoir layers. The growth of the columnar CuO layer produces amorphous grain boundaries between columns. Indeed, the size of the columns is the same as that of the nanowires that form the nanotowers. *So, the nanowires, and thus the nanotowers, are the ultimate form of the columnar growth in our conditions*. Thanks to the strong anisotropy that prevails at low temperature, according to the crystalline orientation of each column, the growth rate will be different, leading to nanowires of different heights. If two adjacent columns have orientations leading to comparable growth rates, the grain

boundary that separates them grows together with them, leading to the presence of an amorphous phase embedded between the two columns. So, we infer that the formation of nanostructures containing crystalline and amorphous phases proceeds this way. In **figure 11**, we can also appreciate how this mechanism applies to CuO nanowalls for Cu–72%Fe alloys. The basement of the wall lies somewhere within layer [CD]. Here, this layer with small grain is thin (It is also visible on SIMS depth-profiles of the Cu–72%Fe alloy, see **supplemental material 4**) but does support the walls, which are not in contact with the Fe_2O_3 sublayer lying underneath. Then, a nanowall would simply be the result of the growth of coalesced columns. This requires:

- a sufficiently high temperature to activate the coalescence of the columns, *i.e.* decreasing the anisotropy by promoting diffusion along one specific new direction. Nanowalls are always observed in the centre of the sample.
- a CuO layer on top, *i.e.* (almost) iron free, even though it is very thin.

The topmost CuO layer is expected to be all the more in tension as the amount of copper increases. Niu *et al.* [6] showed that if the copper concentration increases, the oxidation rate of the alloy decreases. Then, the sublayer with small grains is expected to be thinner at high concentration in iron, thus withstanding better the strain induced by the change in the molar volume between iron and copper oxides. *This might explain the possibility of observing nanowalls at slightly higher radial distance, i.e. slightly lower temperature at high iron concentration.* In the case of CuO nanowires grown from pure copper, the strain is induced by a change in molar volume between CuO (12.4 $cm^3\ mol^{-1}$) and Cu_2O (23.5 $cm^3\ mol^{-1}$). The molar volumes of CuO (12.4 $cm^3\ mol^{-1}$) and Fe_2O_3 (29.9 $cm^3\ mol^{-1}$) differ even more (by a factor of 2.4). This induces buckling, as shown in **figure 7a**. The size of the blistered regions is ~5 µm (**figure 7b**). The case of Cu–10%Fe alloy, where surface patterns are well defined, is chosen here to estimate the order of magnitude of the highest stress level. The buckle diameter d_c of the compressively stressed thin film subjected to buckling reads [35]:

$$d_c = gh\sqrt{\frac{E}{\sigma_c}} \quad (1)$$

where g is the geometric parameter (g ~ 2.2 for an axisymmetric buckle), h the scale thickness, E the oxide elastic modulus, and σ_c the biaxial compressive stress. Substituting in appropriate values: h ~ 2.3 µm and E ~ 82 GPa for CuO [36], we find σ_c ~ 8.4 GPa, which is high but likely.

By introducing iron, the stress level, and then buckling, decreases. CuO nanowalls get smaller and smaller, whereas Fe_2O_3 nanoblades become denser. In **figure 13**, the formation of the different nanostructures is summed up.

4. CONCLUSION

By changing the composition of a Cu–Fe alloy thin film deposited by PVD onto a fused silica substrate, we could observe the formation of original nanostructures after oxidation with an atmospheric plasma afterglow. Besides CuO nanowalls and Fe_2O_3 nanoblades, CuO nanowires and nanotowers were found. These latter nanostructures are characterized by the presence of an amorphous phase trapped between two crystalline walls. No spinel phase could be formed, the treatment temperature being likely too low to permit the synthesis of such a phase.

New experiments are envisaged to see if it is possible to introduce iron and copper into nanostructures made of copper oxide or iron oxide respectively. An additional heater will be necessary to reach temperatures beyond 823 K typically.

ACKNOWLEDGMENTS

The “Centre de compétences X-γ” from the Institut Jean Lamour is gratefully acknowledged for XRD measurements.

REFERENCES

[1] Hasebe, M.; Nishizawa, T. *Calphad* **1980**, *4*, 83–100.

[2] Zhang, P.; Yu, B.; Zhang, L. *Sci. China Ser. B: Chem.* **2009**, *52*, 101–108.

[3] Gesmundo, F.; Niu, Y.; Oquab, D.; Roos, C.; Pieraggi, B.; Viani, F. *Oxidation Metals* **1998**, *49*, 115–146.

[4] Kenfack, F.; Langbein, H. *J. Mater. Sci.* **2006**, *41*, 3683–3693.

[5] Chapelle, A.; Barnabé, A.; Presmanes, L.; Tailhades, *J. Mater. Sci.* **2013**, *48*, 3304–3314.

[6] Niu, Y.; Li, Y.S.; Gesmundo, F. Corros. Sci. **2000**, *42*, 165–181.

[7] Li, Y.S.; Niu, Y.; Gesmundo, F.; Wang, F.H. *Corros. Sci.* **2002**, *44*, 1457–1468.

[8] Zhu, Y.; Sow, C.-H.; Yu, T.; Zhao, Q.; Li, P.; Shen, Z.; Yu, D.; Thong, J. T.-L. *Adv. Funct. Mater.* **2006**, *16*, 2415–2422.

[9] Yue, Y.; Chen, M.; Ju, Y.; Zhang, L. *Scr. Mater.* **2012**, *66*, 81–84.

[10] Kumar, A.; Srivastava, A.K.; Tiwari, P.; Nandedkar, R.V. *J. Phys.: Condens. Matter* **2004**, *16*, 8531–8543.

[11] Ostrikov, K.; Neyts, E.C.; Meyyappan, M. *Adv. Phys.* **2013**, *62*, 113–224.

[12] Cheng, Q.; Yan, W.; Randeniya, L.; Zhang, F.; Ostrikov, K. *J. Appl. Phys.* **2014**, *115*, 124310.

[13] Cvelbar, U. *J. Phys. D: Appl. Phys.* **2011**, *44*, 174014.

[14] Cvelbar, U.; Ostrikov, K.; Levchenko, I.; Mozetic, M.; Sunkara, M. K. *Appl. Phys. Lett.* **2009**, *94*, 211502.

[15] Ostrikov, K. K.; Levchenko, I.; Cvelbar, U.; Sunkara, M.; Mozetic, M. *Nanoscale* **2010**, *2*, 2012–2027.

[16] Wan, Y.T.; Liu, J.Y.; Li, W.; Meng, F.L.; Jin, Z.; Yu, X.Y.; Huang, X.J.; Liu, J.H. *Nanotechnol.* **2011**, *22*, 315501.

[17] Liu, X.; Wu, X.H.; Cao, H.; Chang, R.P.H. *J. Appl. Phys.* **2004**, *95*, 3141–3147.

[18] Mariotti, D.; Bose, A. C.; Ostrikov, K. *IEEE Trans. Plasma Sci.* **2009**, *37*, 1027–1033.

[19] Sharma, S.; Sunkara, M. K. *J. Am. Chem. Soc.* **2002**, *124*, 12288–12293.

[20] Chen, C.; Bai, H.; Chang, S. M.; Chang, C.; Den, W *J. Nanopart. Res.* **2007**, *9*, 365-375.

[21] Altaweel, A.; Filipič, G.; Gries, T.; Belmonte, T. *J. Cryst. Growth* **2014**, *407*, 17–24.

[22] Arnoult, G.; Cardoso, R.P.; Belmonte, T.; Henrion, G. *Appl. Phys. Lett.* **2008**, *93*, 191507.

[23] Arnoult, G.; Belmonte, T.; Kosior, F.; Dossot, M.; Henrion, G. *J. Phys. D: Appl. Phys.* **2011**, *44*, 174022.

[24] Arnoult, G.; Belmonte, T.; Henrion, G. *Appl. Phys. Lett.* **2010**, *96*, 101505.

[25] Kuete Saa, D.; Cardoso, R.P.; Kosior, F.; Altaweel, A.; Gries, T.; Laminsi, S.; Belmonte T. *Surf. Coat. Technol.* **2014**, *255*, 3–7.

[26] Arnoult, G.; Gries, T.; Henrion, G.; Migot, S.; Fournée, V.; Belmonte, T. *Plasma Process. Polym.* **2012**, *9*, 1125–1131.

[27] Sova, R. M.; Linevsky, M. J.; Thomas, M. E.; Mark, F. F. *Infrared Phys. Technol.* **1998**, *39*, 2517–261.

[28] Wen, X.; Wang, S.; Ding, Y.; Wang, Z. L.; Yang, S. *J. Phys. Chem. B* **2005**, *109*, 215–220.

[29] Choopun, S.; Hongsith, N.; Wongrat, E. *Metal-oxide Nanowires by Thermal Oxidation Reaction Technique* Chapter 5 in "Nanowires"; Ed. by Paola Prete, March **2010**, INTECH; Croatia

[30] Li, B.; Cao, Y.-P.; Feng, X.-Q.; Gao, H. *Soft Matter* **2012**, *8*, 5728–5745.

[31] Chen, M.; Yue, Y.; Ju, Y. *J. Appl. Phys.* **2012**, *111*, 104305.

[32] Voss, D.A.; Butler, E.P.; Mitchell, T.E. *Metall. Trans. A* **1998**, *13A*, 929–935.

[33] Takagi, R. *J. Phys. Soc. Jap.* **1957**, *12*, 1212–1218.

[34] Bertrand, N.; Desgranges, C.; Poquillon, D.; Lafont, M. C.; Monceau, D. *Oxid. Met.* **2010**, *73*, 139–162.

[35] Tolpygo, V. K.; Clarke, D. R. *Acta Mater.* **1998**, *46*, 5167–5174.

[36] Tan, E. P. S.; Zhu, Y.; Yu, T.; Dai, L.; Sow, C. H.; Tan, V. B. C.; Lim, C. T. *Appl. Phys. Lett.* **2007**, *90*, 163112.

CAPTIONS

Figure 1: a) Experimental set-up. b) Picture of the afterglow operating at atmospheric pressure. c) Picture of the treated sample.

Figure 2: SEM images of oxides nanostructures grown by afterglow-assisted oxidation of pure metals at various radial distances.

Figure 3: Map of as-grown nanostructures as a function of the radial distance for different alloy compositions. Fe_2O_3 nanoblades are found as well as three different types of CuO nanostructures: nanowalls, nanotowers and nanowires. For alloy compositions with less than 72% Fe, stress-induced patterns are observed (grey area).

Figure 4: TEM and high-resolution SEM images of the four types of oxides nanostructures grown by afterglow-assisted oxidation.

Figure 5: a) General view of nanowires by TEM. b) Example of a single nanotower, showing darker and brighter areas. c) Magnification of contrasted area. d) high-resolution image showing that the darker area is well crystallized, whereas the brighter area is amorphous and contains isolated nanocrystals (circle).

Figure 6: EDX mapping obtained by TEM of CuO nanowires (90%Cu-10%Fe sample) showing the bright-field image (BF on the top left), and the abundance of copper, oxygen and iron. We observe that the iron signal is very weak, but not completely negligible, on the wire.

Figure 7: a) cross view of the patterns obtained after treatment of a Fe-90%Cu layer. b) Top view of the same sample. c) Magnification of the darker transition between two lighter areas.

Figure 8: a) Normalized intensities of Cu (red line), Fe (black line) and O (blue line) SIMS signals as a function of depth for various radial distances. Depth, expressed in sputtering time, was rescaled to set to 0 the position of the silica surface. b) Back-scattered electron image of the oxidized layer observed in cross-section at the centre (radial distance = +0.0 mm). Alloy with 34%Fe treated for 2 hours.

Figure 9: Microstructure of the oxide layers together with the corresponding SIMS depth-profile for an alloy with 34%Fe treated for 2 h. +1 mm from the centre of the treatment. a) and b) are magnifications of the figure on the upper-right showing the roots of the nanowires within the columnar layer.

Figure 10: Microstructure of the oxide layers together with the corresponding SIMS depth-profile for an alloy with 90%Fe treated for 2 h.

Figure 11: CuO nanowalls growing among nanowires. The nanowalls grow directly on the sublayer with large grains. Alloy with 72%Fe treated for 2 hours.

Figure 12: Fe_2O_3 nanoblades growing among CuO nanowalls. Cu-Fe alloy containing 72%Fe and oxidized for two hours.

Figure 13: Proposed growth mechanism of Fe_2O_3 nanoblades and CuO nanostructures.

Supplemental Material 1: a) Infrared camera images recorded at increasing times from 1 to 6. b) Rear side temperature as determined by IR camera measures as a function of the radial distance (case of a silica substrate covered by 900 nm thick Fe-Cu layer). The steady-state value is reached after ~300 s.

Supplemental Material 2: Micro-Energy Dispersive Spectroscopy analyses of a CuO nanowires. Traces of iron (less than 1 at.%) are detected.

Supplemental Material 3: XRD patterns of oxidized alloys for different compositions. No spinel phase is observed.

Supplemental Material 4: Normalized intensities of Cu (red line), Fe (black line) and O (blue line) SIMS signals as a function of depth for various radial distances.

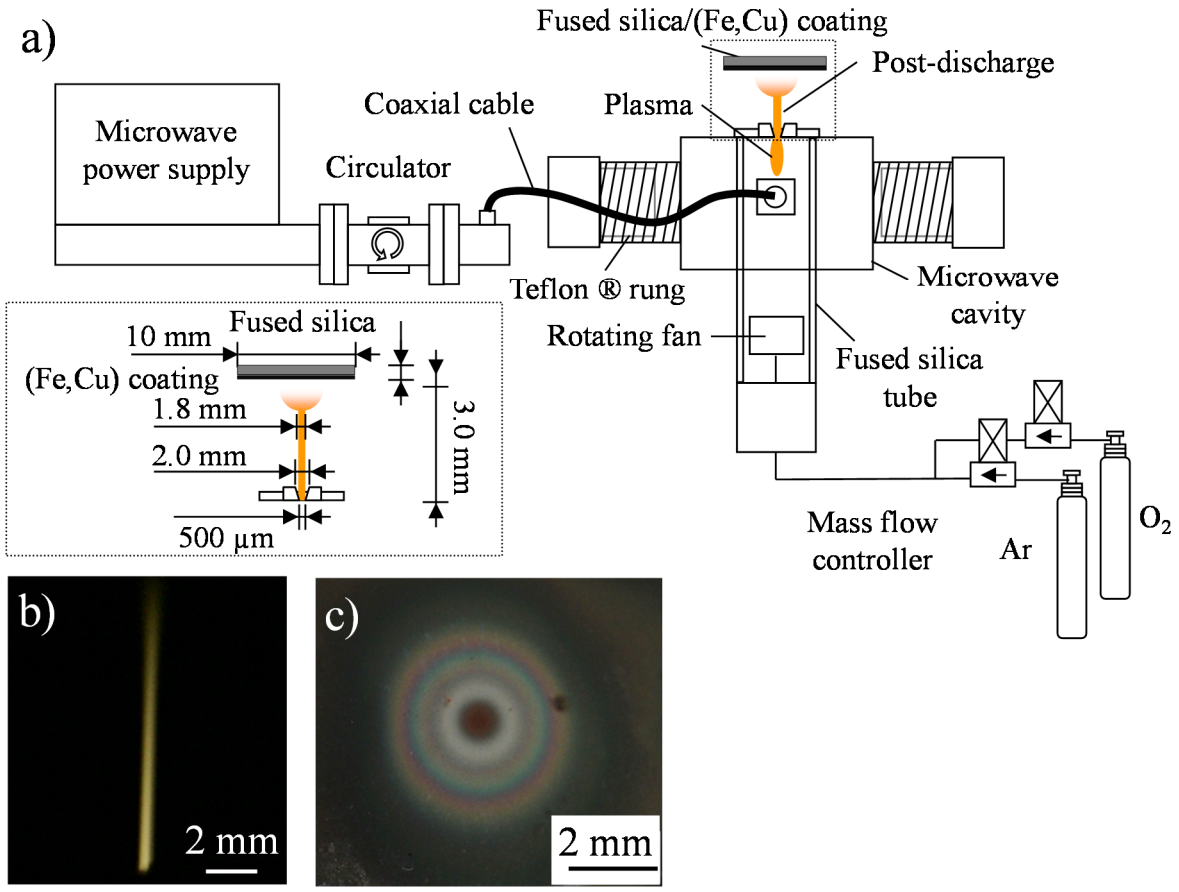

Figure 1: a) Experimental set-up. b) Picture of the afterglow operating at atmospheric pressure. c) Picture of the treated sample.

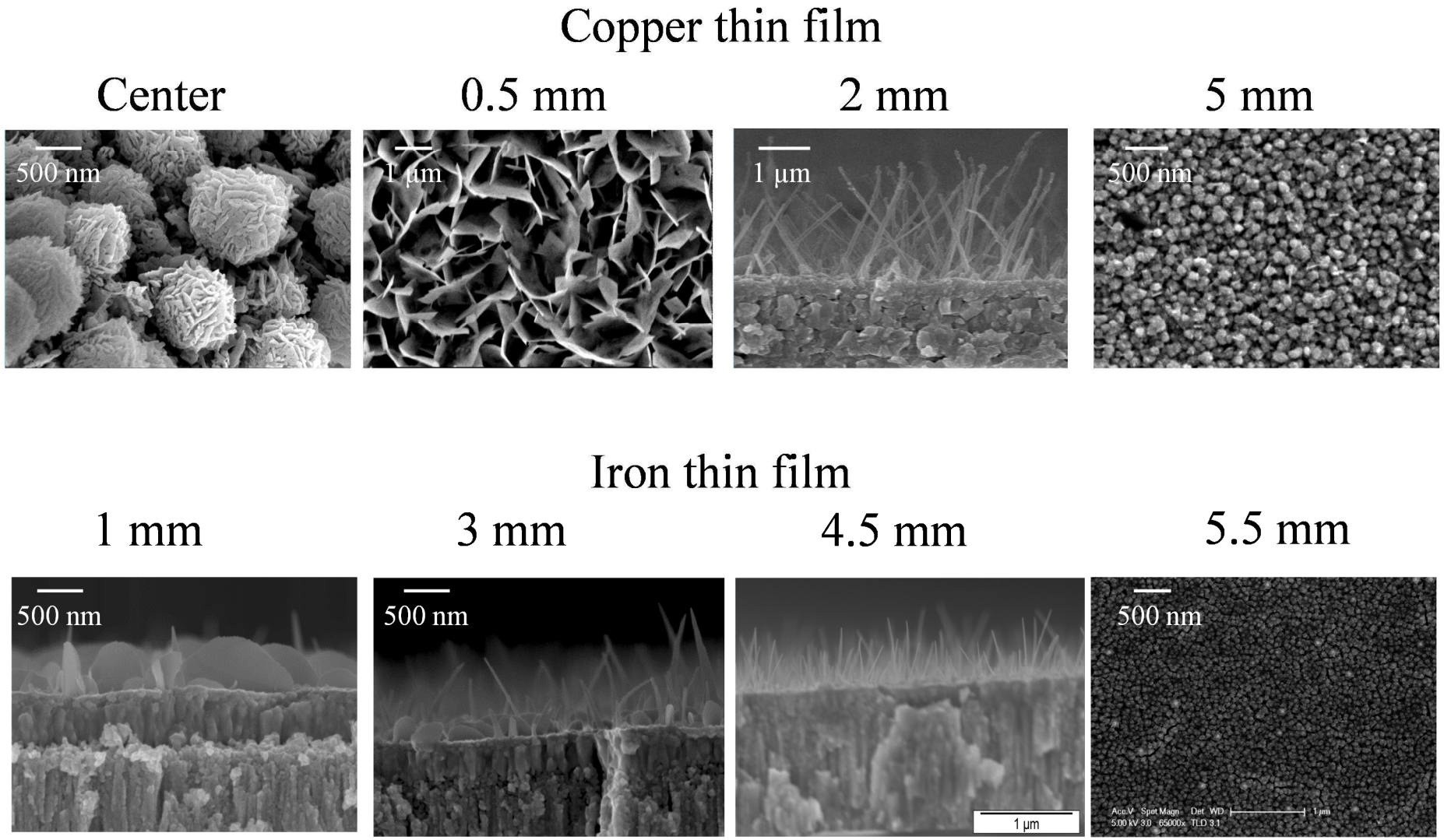

Figure 2: SEM images of oxides nanostructures grown by afterglow-assisted oxidation of pure metals at various radial distances.

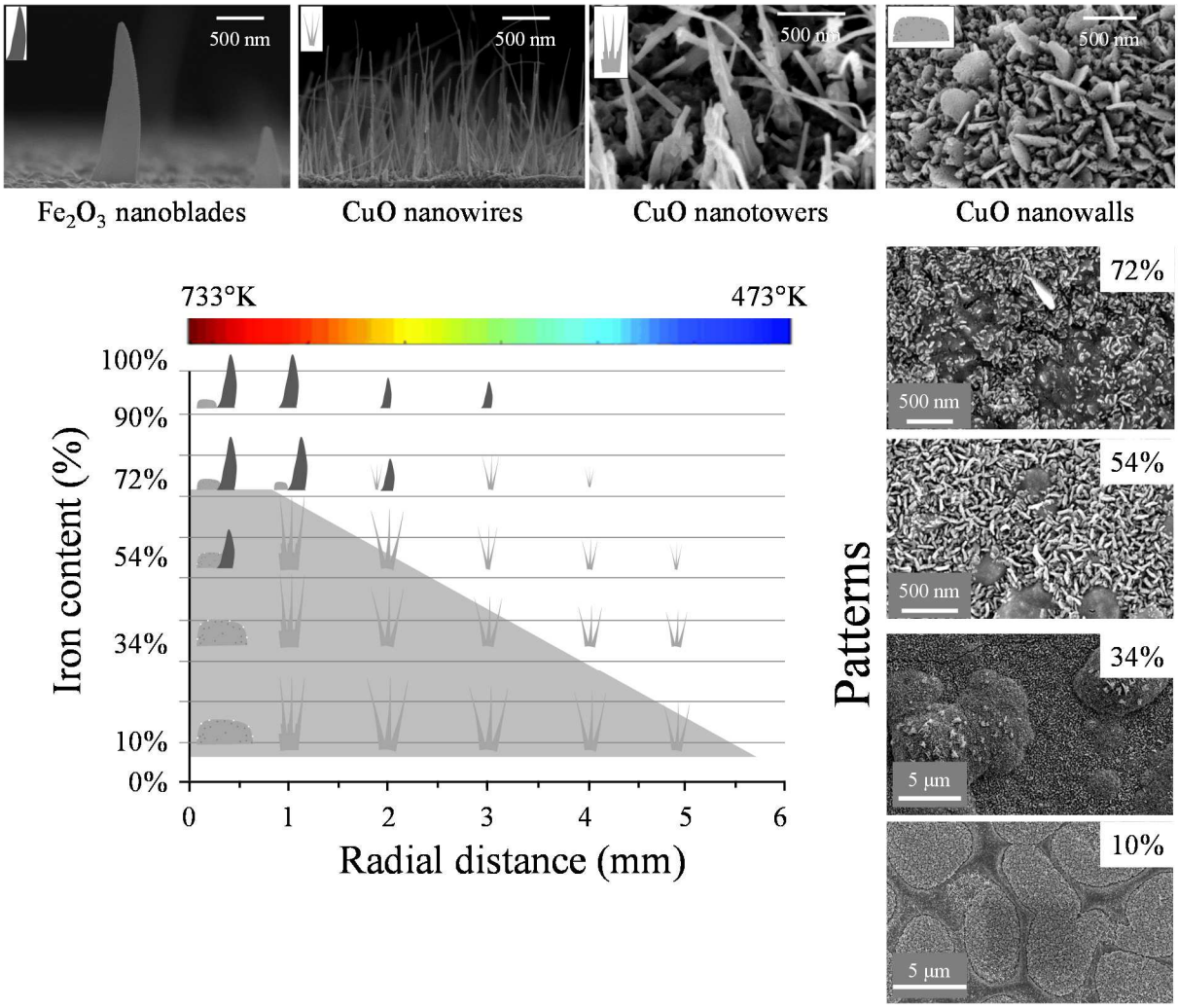

Figure 3: Map of as-grown nanostructures as a function of the radial distance for different alloy compositions. Fe_2O_3 nanoblades are found as well as three different types of CuO nanostructures: nanowalls, nanotowers and nanowires. For alloy compositions with less than 72% Fe, stress-induced patterns are observed (grey area).

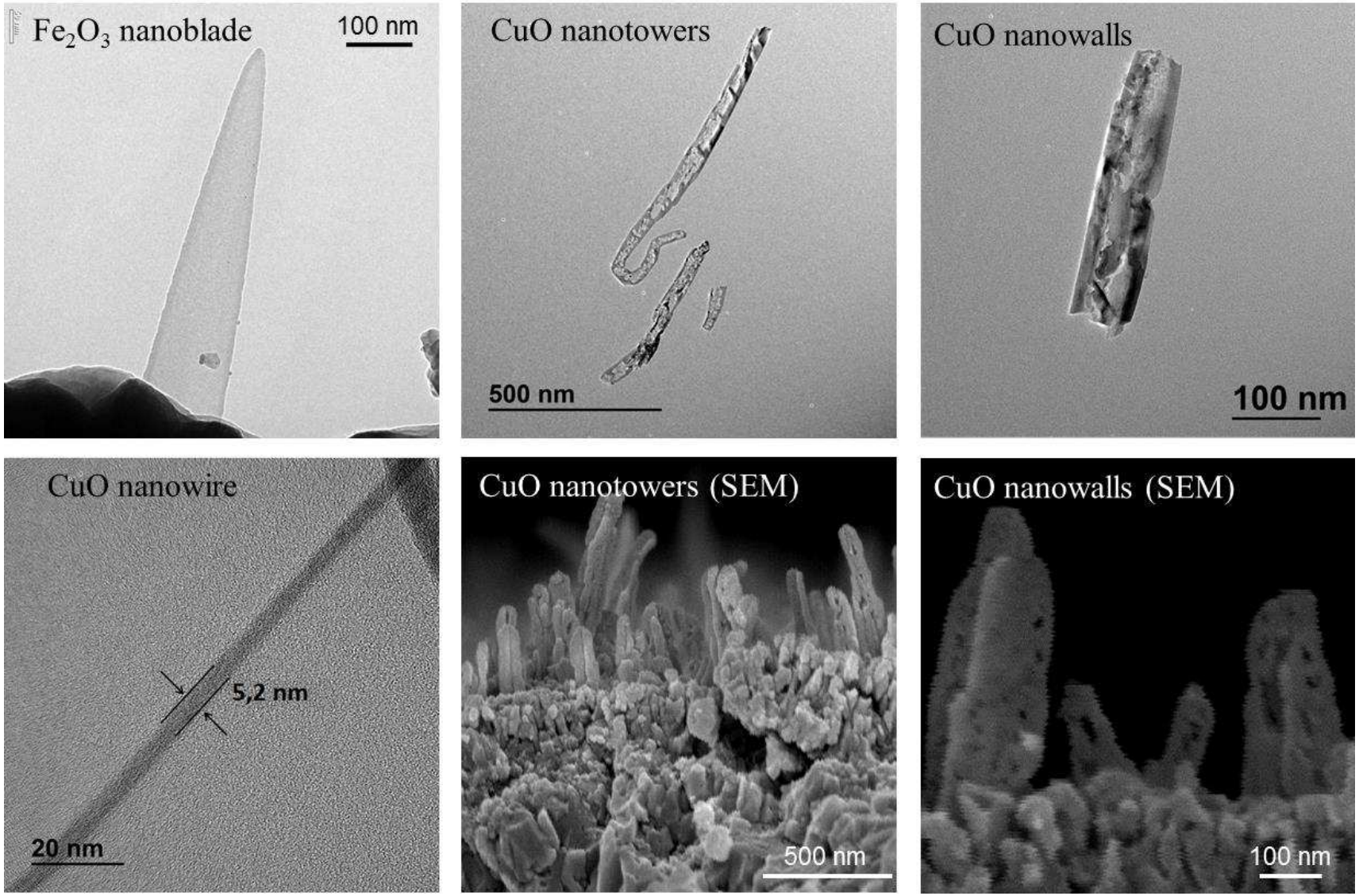

Figure 4: TEM and high-resolution SEM images of the four types of oxides nanostructures grown by afterglow-assisted oxidation.

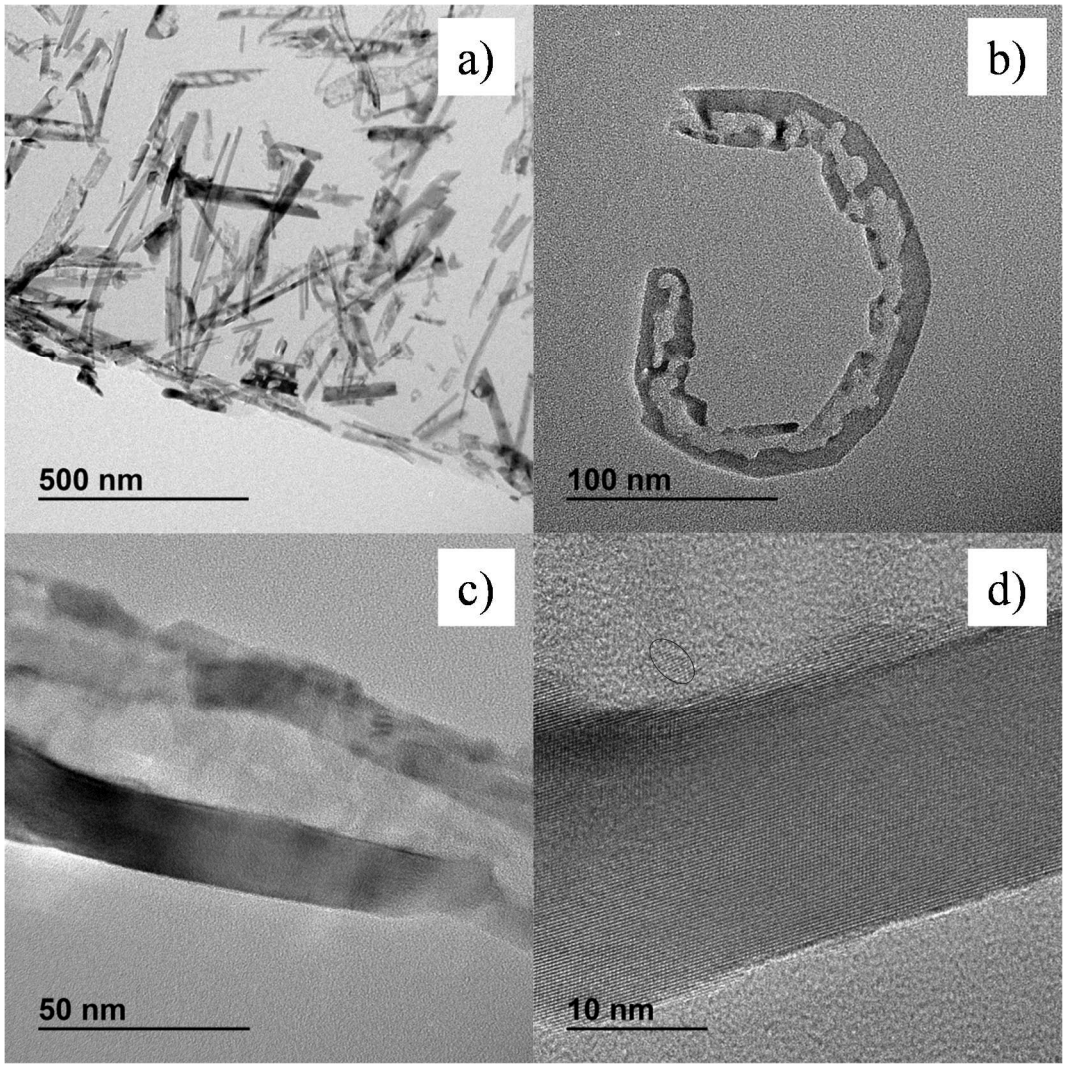

Figure 5: a) General view of nanowires by TEM. b) Example of a single nanotower, showing darker and brighter areas. c) Magnification of contrasted area. d) high-resolution image showing that the darker area is well crystallized, whereas the brighter area is amorphous and contains isolated nanocrystals (circle).

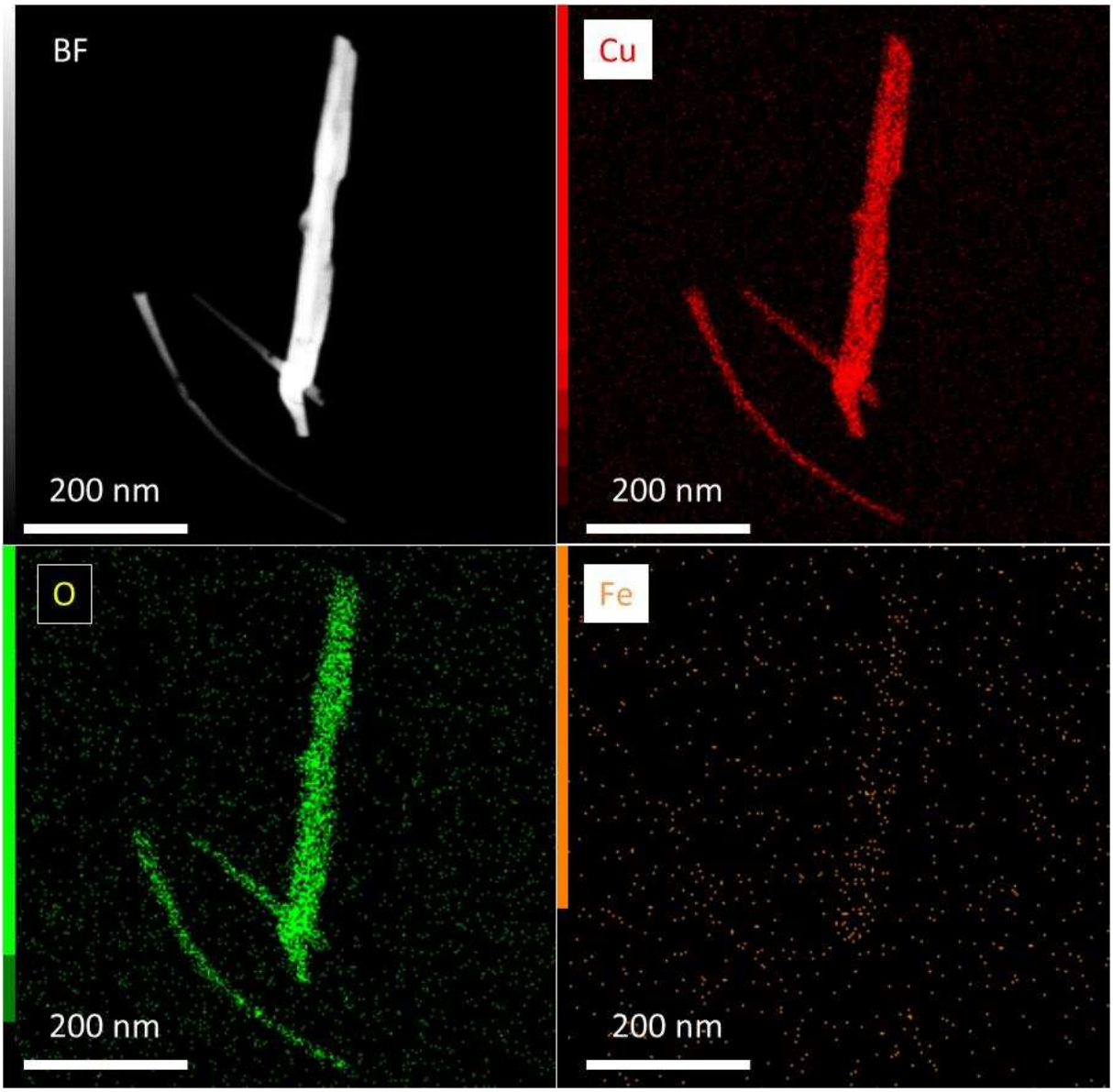

Figure 6: EDX mapping obtained by TEM of CuO nanowires (90%Cu-10%Fe sample) showing the bright-field image (BF on the top left), and the abundance of copper, oxygen and iron. We observe that the iron signal is very weak, but not completely negligible, on the wire.

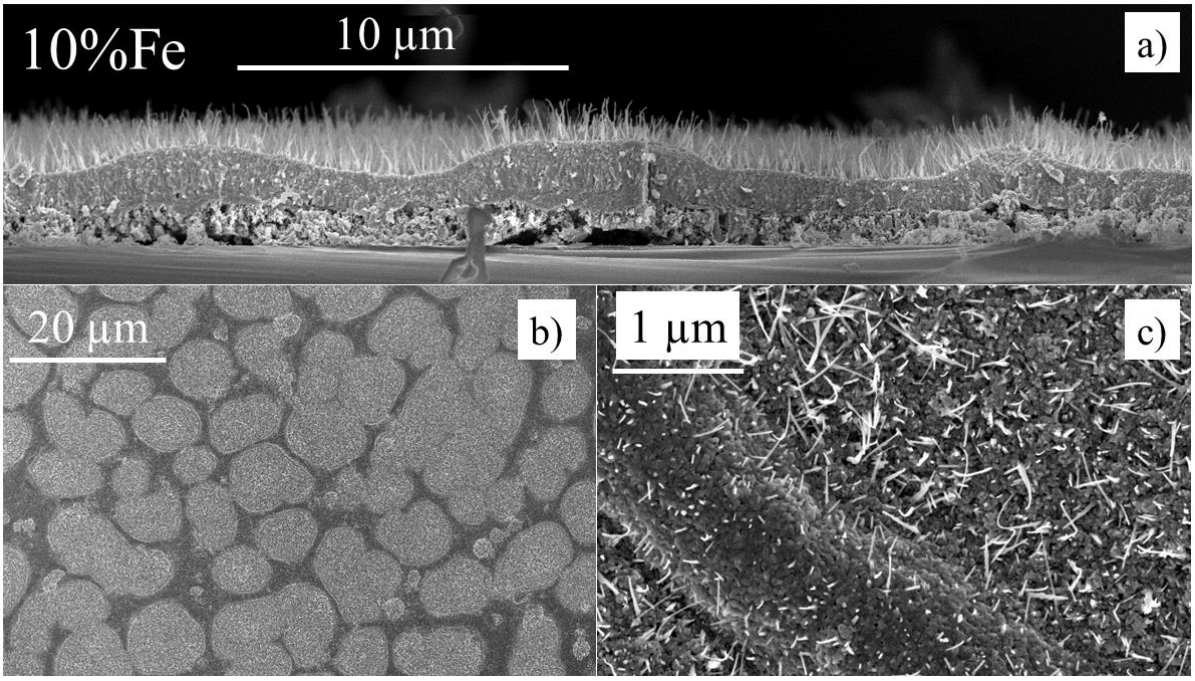

Figure 7: a) cross view of the patterns obtained after treatment of a Fe-90%Cu layer. b) Top view of the same sample. c) Magnification of the darker transition between two lighter areas.

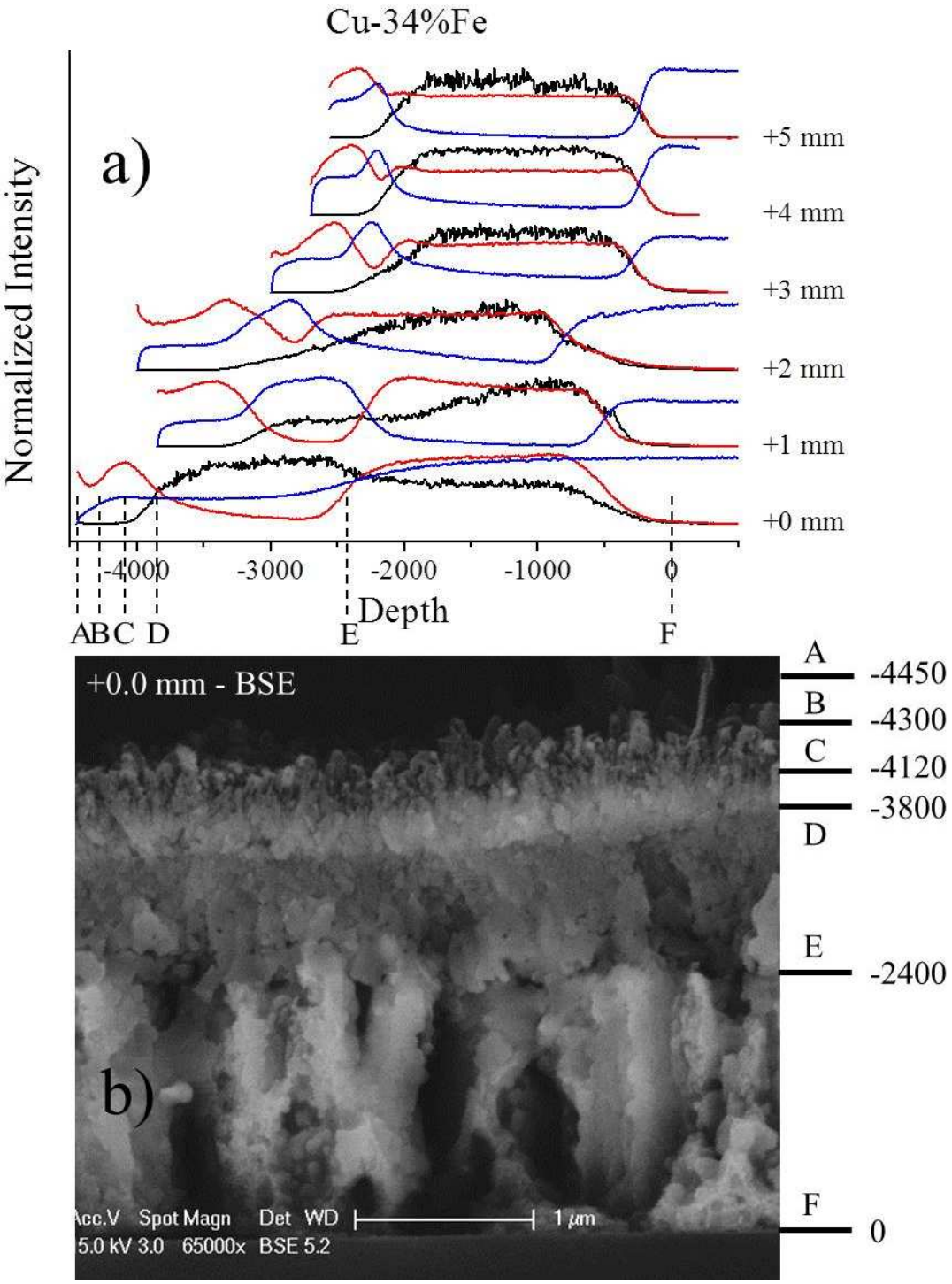

Figure 8: a) Normalized intensities of Cu (red line), Fe (black line) and O (blue line) SIMS signals as a function of depth for various radial distances. Depth, expressed in sputtering time, was rescaled to set to 0 the position of the silica surface. b) Back-scattered electron image of the oxidized layer observed in cross-section at the centre (radial distance = +0.0 mm). Alloy with 34%Fe treated for 2 hours.

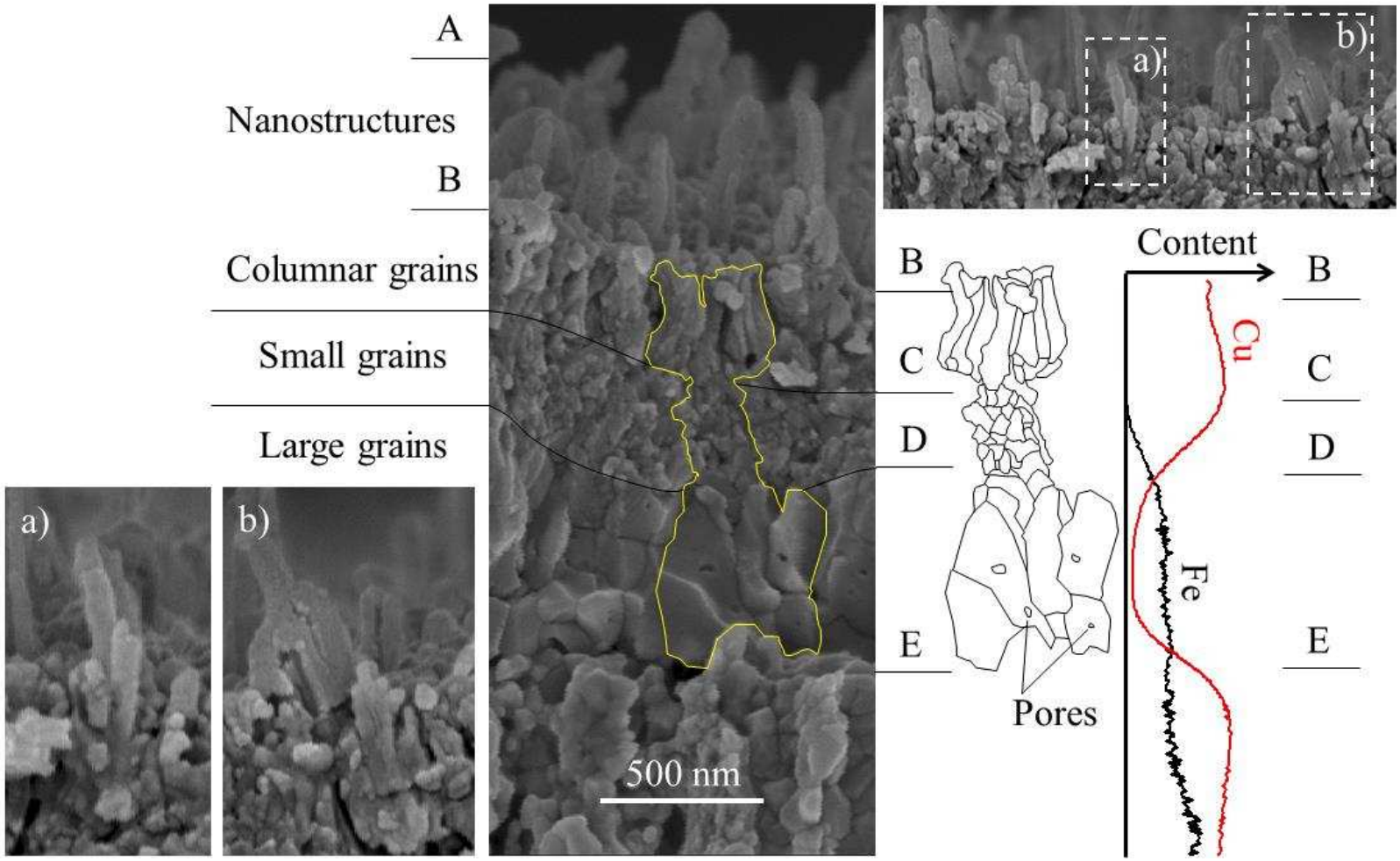

Figure 9: Microstructure of the oxide layers together with the corresponding SIMS depth-profile for an alloy with 34%Fe treated for 2 h. +1 mm from the centre of the treatment. a) and b) are magnifications of the figure on the upper-right showing the roots of the nanowires within the columnar layer.

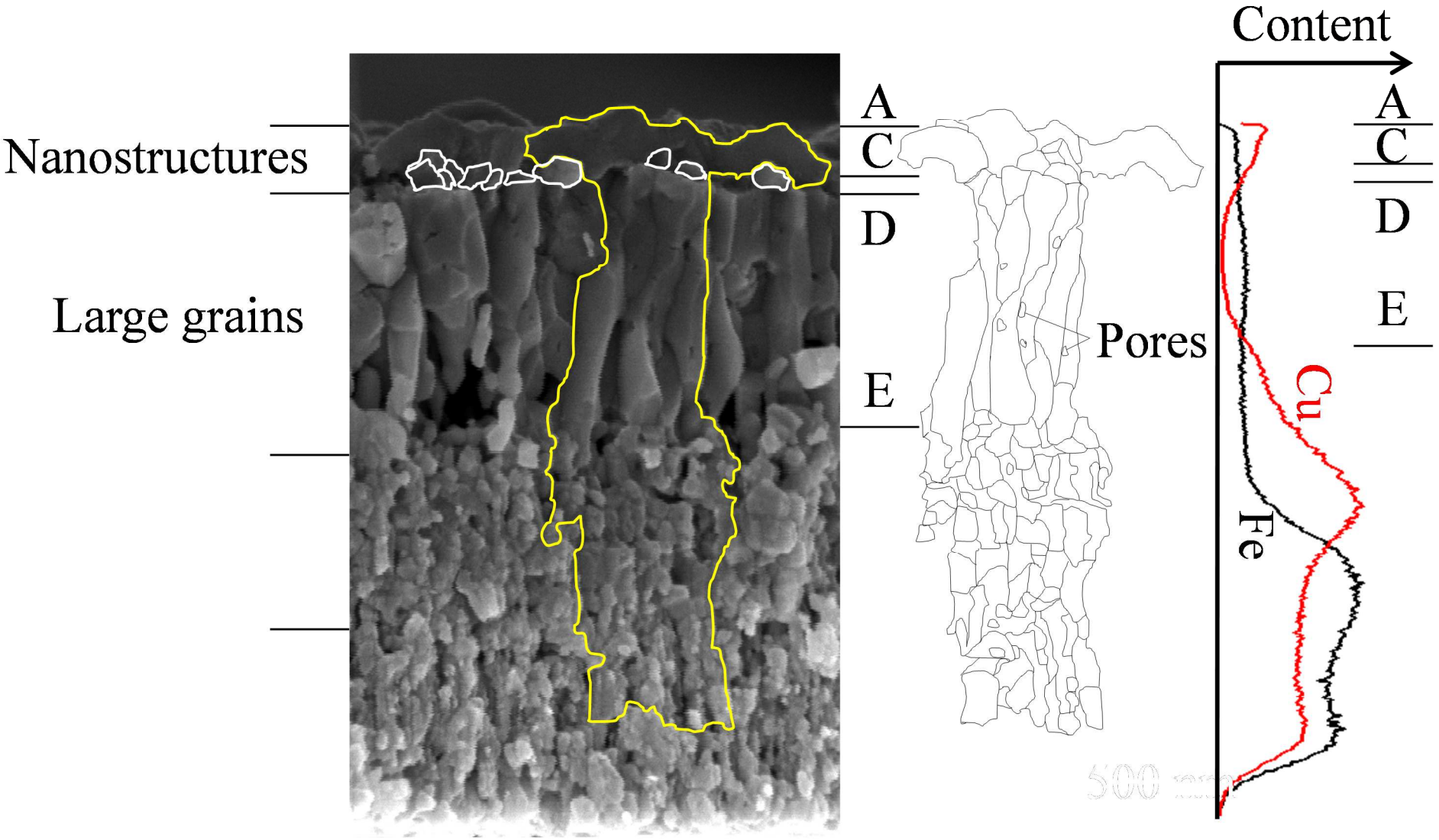

Figure 10: Microstructure of the oxide layers together with the corresponding SIMS depth-profile for an alloy with 90%Fe treated for 2 h.

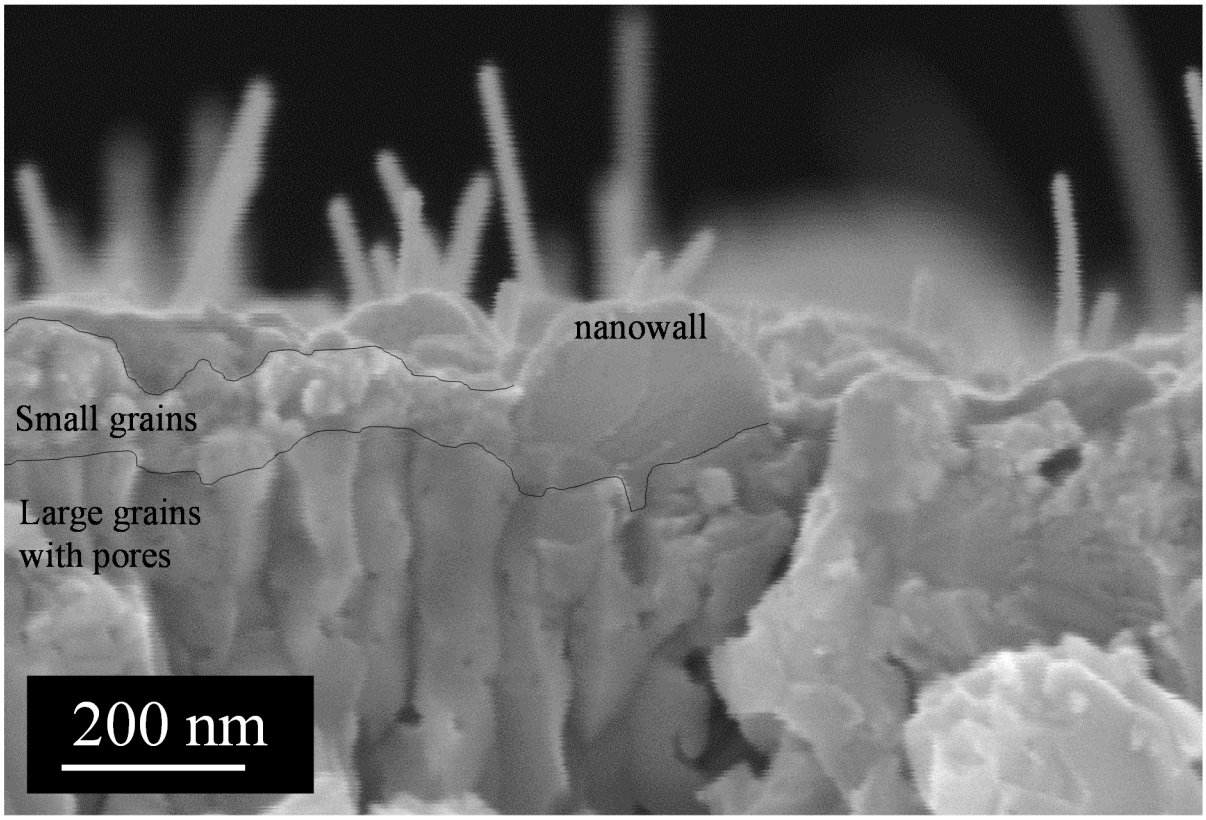

Figure 11: CuO nanowalls growing among nanoblades. The nanowalls grow directly on the sublayer with large grains. Alloy with 72%Fe treated for 2 hours.

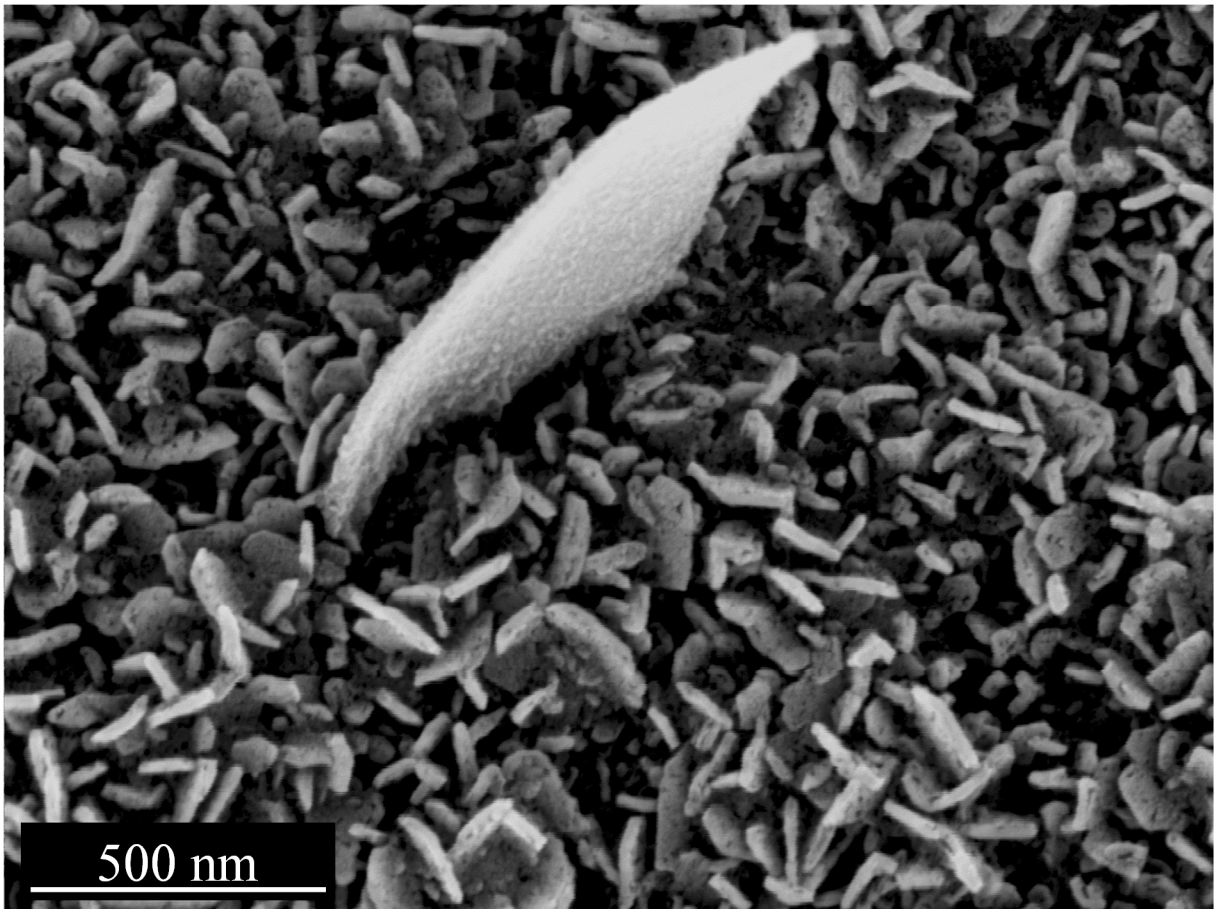

Figure 12: Fe_2O_3 nanoblades growing among CuO nanowalls. Cu-Fe alloy containing 72%Fe and oxidized for two hours.

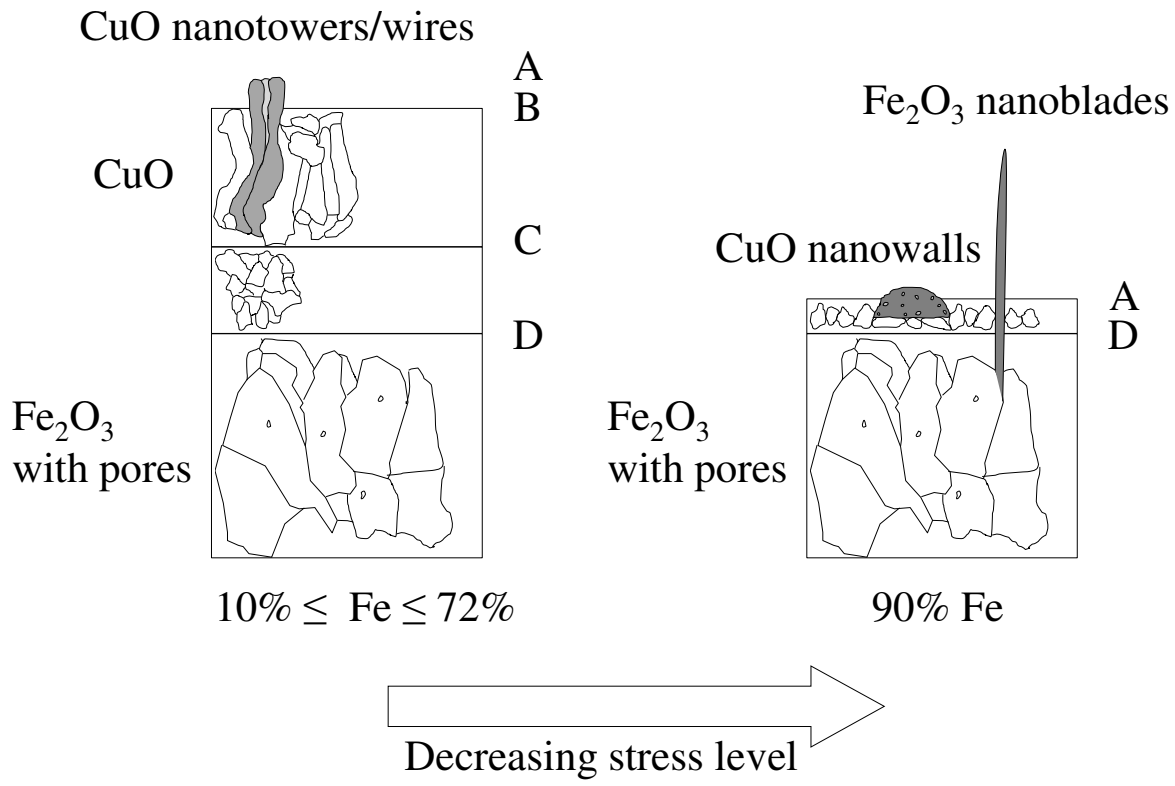

Figure 13: Proposed growth mechanism of Fe_2O_3 nanoblades and CuO nanostructures.

SUPPORTING INFORMATION

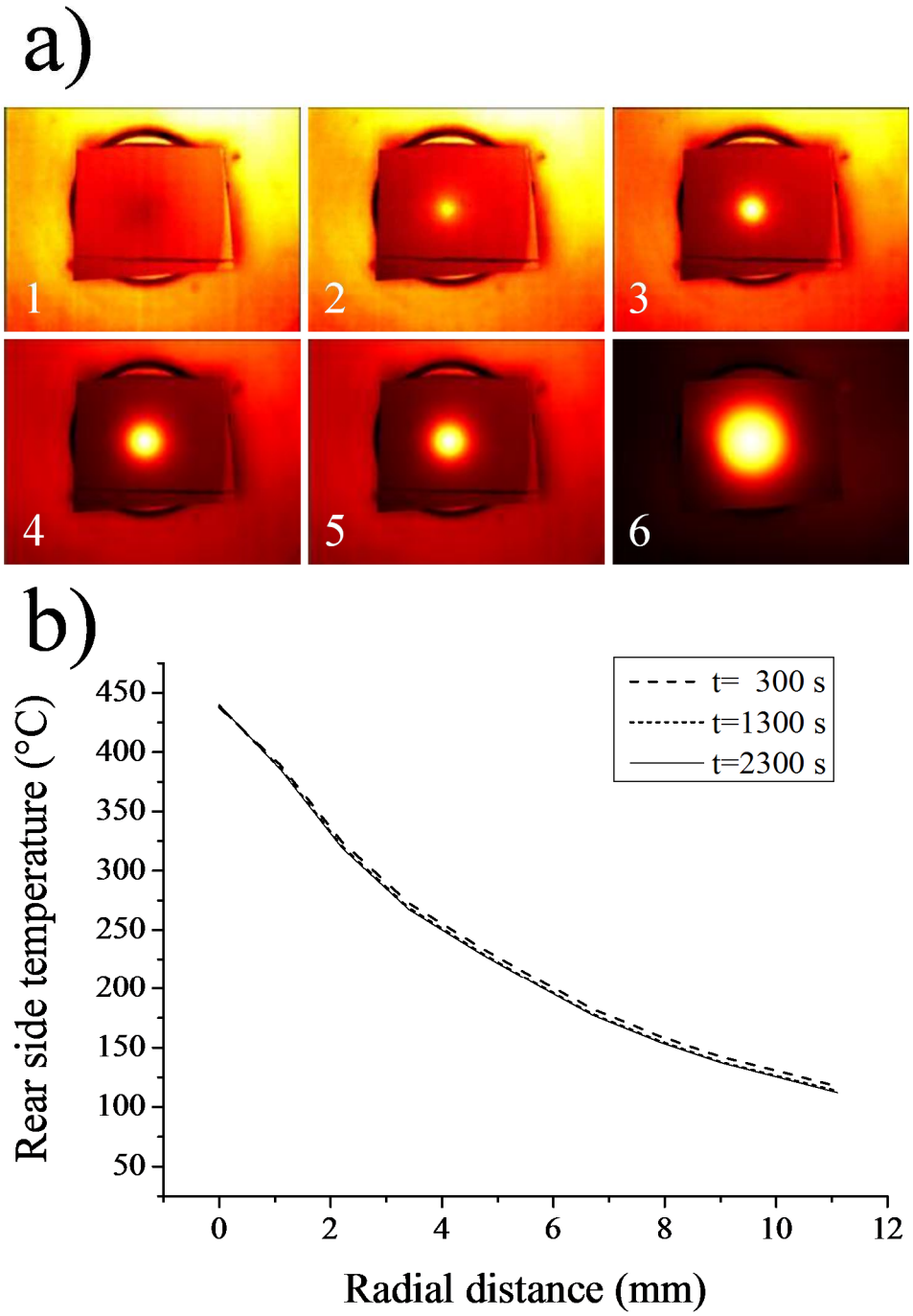

Supplemental Material 1: a) Infrared camera images recorded at increasing times (every 25 s) from 1 to 6. b) Rear side temperature as determined by IR camera measures as a function of the radial distance (case of a silica substrate covered by 900 nm thick Fe-Cu layer). The steady-state value is reached after ~300 s.

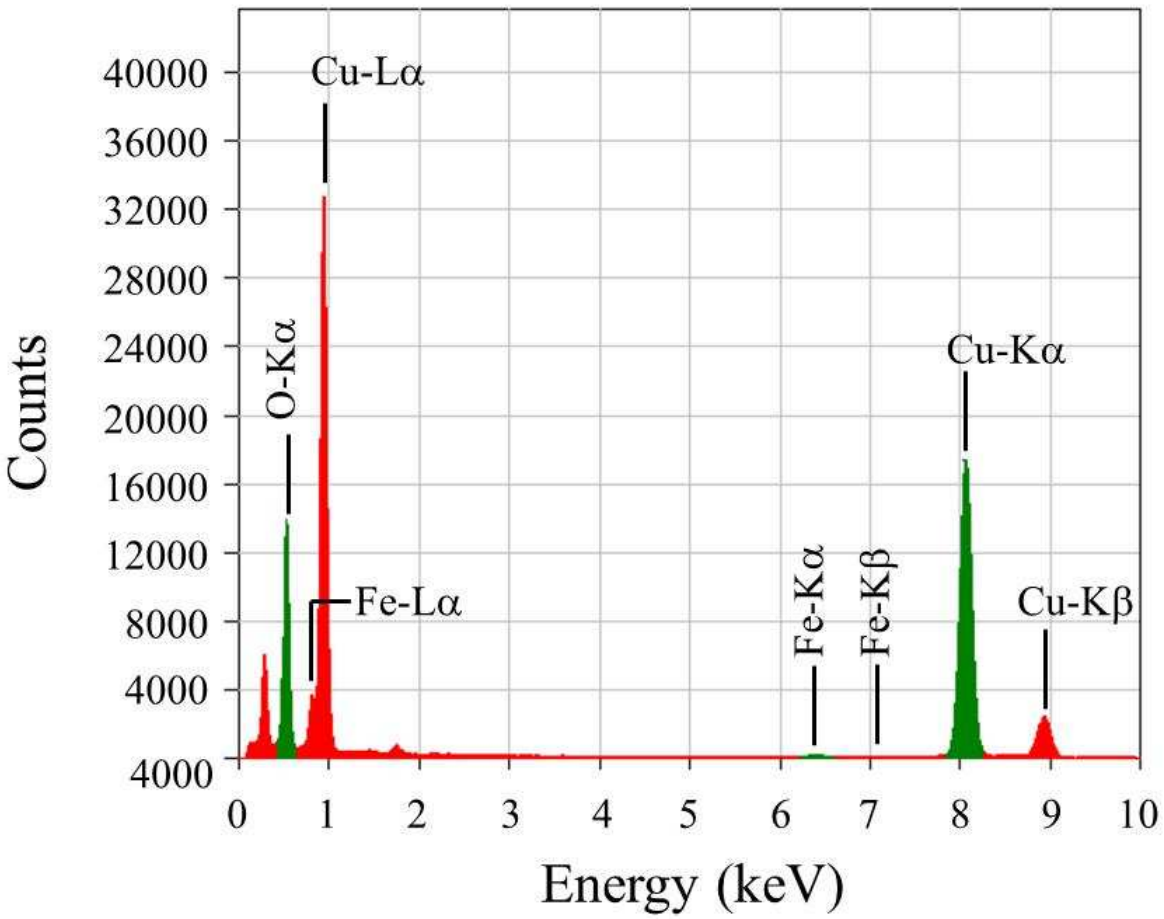

Supplemental Material 2: Micro-Energy Dispersive Spectroscopy analyses of a CuO nanowires. Traces of iron (less than 1 at.%) are detected.

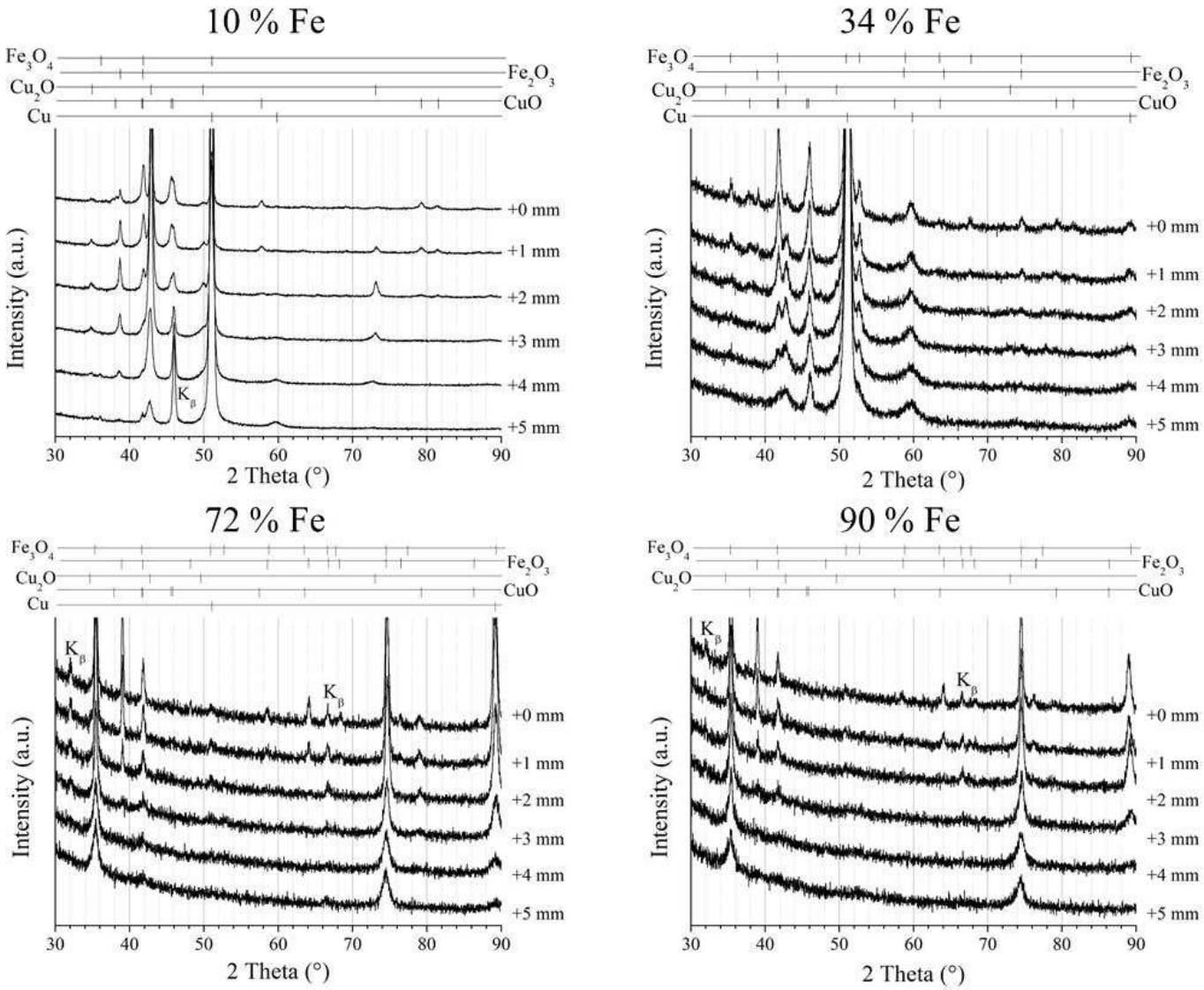

Supplemental Material 3: XRD patterns of oxidized alloys for different compositions. No spinel phase is observed.

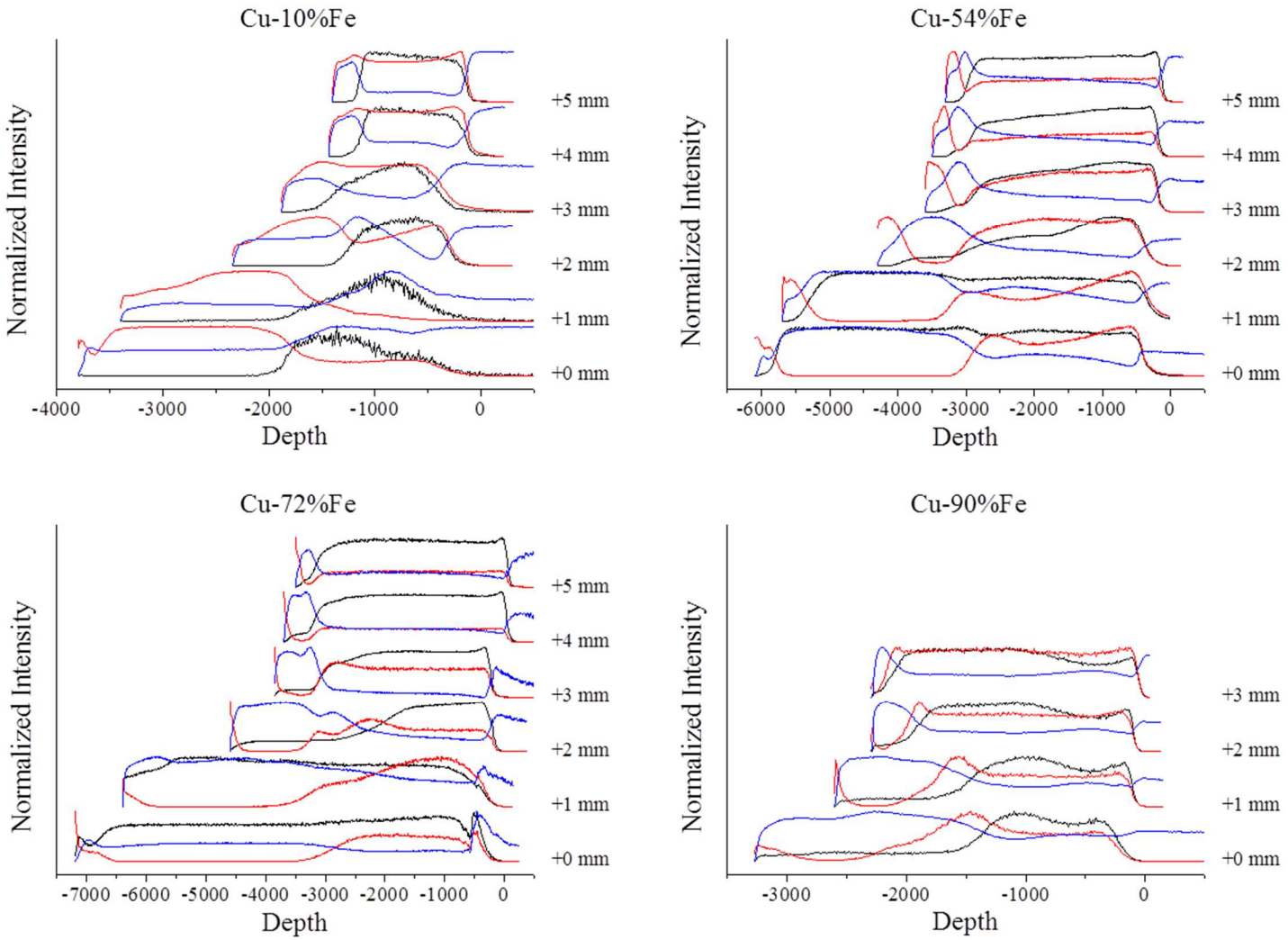

Supplemental Material 4: Normalized intensities of Cu (red line), Fe (black line) and O (blue line) SIMS signals as a function of depth for various radial distances.